

REPORT DOCUMENTATION PAGE

Form Approved
OMB No. 0704-0188

Public reporting burden for this collection of information is estimated to average 1 hour per response, including the time for reviewing instructions, searching existing data sources, gathering and maintaining the data needed, and completing and reviewing the collection of information. Send comments regarding this burden estimate or any other aspect of this collection of information, including suggestions for reducing this burden to Washington Headquarters Services, Directorate for Information Operations and Reports, 1215 Jefferson Davis Highway, Suite 1204, Arlington, VA 22202-4302, and to the Office of Management and Budget, Paperwork Reduction Project (0704-0188), Washington, DC 20503.

1. AGENCY USE ONLY (Leave Blank)		2. REPORT DATE 24 June 1999	3. REPORT TYPE AND DATES COVERED 10/98-9/99
4. TITLE AND SUBTITLE Phase Transitions in Vapor Deposited Water under the Influence of High Surface Electric Fields			5. FUNDING NUMBERS N00014-97-1-0417 Richard Carlin
6. AUTHOR(S) D. L. Scovell, T. D. Pinkerton, V. K. Medvedev, and E. M. Stuve			
7. PERFORMING ORGANIZATION NAME(S) AND ADDRESS(ES) University of Washington Department of Chemical Engineering Box 351750 Seattle, WA 98195-1750			8. PERFORMING ORGANIZATION REPORT NUMBER Technical Report No. 11
9. SPONSORING / MONITORING AGENCY NAME(S) AND ADDRESS(ES) Office of Naval Research 800 N. Quincy Street Arlington, VA 22217			10. SPONSORING/MONITORING AGENCY REPORT NUMBER
11. SUPPLEMENTARY NOTES Prepared for publication in Surface Science			
12a. DISTRIBUTION / AVAILABILITY STATEMENT This document has been approved for public release and sale; its distribution is unlimited.			12b. DISTRIBUTION CODE 19990701 049
13. ABSTRACT (Maximum 200 words) Field ionization of vapor deposited water on a platinum field emitter was studied over a temperature range of 103 -150 K. Water adlayers that were 50 - 3600 Å thick were grown under field-free conditions by exposure of a cryogenically cooled emitter tip to water vapor in ultrahigh vacuum. Field ionization was probed by ramped field desorption (RFD) in which desorption of ionic species (hydrated protons) is measured while increasing the applied electric field linearly in time. The dependence of the field required for ionization onset as a function of temperature and water thickness is presented and discussed. In the limit of thin layers the onset field decreased from 0.5 to 0.2 V/Å as temperature increased from 105 to 150 K. An activation barrier of 0.7 eV (16 kcal/mol) for ionization of amorphous and crystalline water was estimated from the temperature dependence of the onset field. This is in excellent agreement with the 0.74 eV (17 kcal/mol) required to produce a pair of ions from a pair of solvated water molecules.			
14. SUBJECT TERMS Water, Field ionization, Platinum, Water ionization, Electric field effects, Amorphous solid water, Crystalline water			15. NUMBER OF PAGES 34
			16. PRICE CODE
17. SECURITY CLASSIFICATION OF REPORT Unclassified	18. SECURITY CLASSIFICATION OF THIS PAGE Unclassified	19. SECURITY CLASSIFICATION OF ABSTRACT Unclassified	20. LIMITATION OF ABSTRACT

OFFICE OF NAVAL RESEARCH

Research Contract N00014-97-1-0417

Program Manager Richard Carlin

Technical Report No. 11

**"Phase Transitions in Vapor Deposited Water under the
Influence of High Surface Electric Fields"**

by

**D. L. Scovell, T. D. Pinkerton, V. K. Medvedev,
and E. M. Stuve**

Prepared for Publication

in

Surface Science

**University of Washington
Department of Chemical Engineering
Box 351750
Seattle, WA 98195-1750**

June, 1999

Reproduction in whole, or in part, is permitted for any purpose of the United States Government.

This document has been approved for public release and sale; its distribution is unlimited.

**PHASE TRANSITIONS IN VAPOR DEPOSITED WATER
UNDER THE INFLUENCE OF HIGH SURFACE ELECTRIC FIELDS**

Dawn L. Scovell, Tim D. Pinkerton, Valentin K. Medvedev, and Eric M. Stuve*

University of Washington
Department of Chemical Engineering
Box 351750
Seattle, WA 98195

Telephone: (206) 543 - 5467
FAX: (206) 543 - 3778
e-mail: stuve@u.washington.edu

Submitted to: Surface Science

Date: 9 June 1999

ABSTRACT

Field ionization of vapor deposited water on a platinum field emitter was studied over a temperature range of 103 -150 K. Water adlayers that were 50 – 3600 Å thick were grown under field-free conditions by exposure of a cryogenically cooled emitter tip to water vapor in ultrahigh vacuum. Field ionization was probed by ramped field desorption (RFD) in which desorption of ionic species (hydrated protons) is measured while increasing the applied electric field linearly in time. The dependence of the field required for ionization onset as a function of temperature and water thickness is presented and discussed. In the limit of thin layers the onset field decreased from 0.5 to 0.2 V/Å as temperature increased from 105 to 150 K. An activation barrier of 0.7 eV (16 kcal/mol) for ionization of amorphous and crystalline water was estimated from the temperature dependence of the onset field. This is in excellent agreement with the 0.74 eV (17 kcal/mol) required to produce a pair of ions from a pair of solvated water molecules.

Instructions for Authors Concerning the Use of Keywords for Indexing in Surface Science

Given below is a listing of keywords for the Subject and Materials Indexes used by Surface Science. The Subject index is divided into three classes: Theoretical Methods, Experimental Methods, and Phenomena. Please indicate below your abstract at least one keyword from as many of the three classes as appropriate to describe the contents of your manuscript. (You may also tick the appropriate box and include this list with your manuscript). Occasionally it will not be possible to include a keyword from all three classes, e.g. a general theory manuscript will not exhibit a keyword from the Experimental Methods class. In such a case, omit the entry from the inapplicable class. Also, if appropriate, please select a keyword from one of the three classes of the Materials Index, i.e. Elemental and Chemical Identity, Physical State, and Electrical and Magnetic Behavior. You may use multiple keywords in the above mentioned six classes up to a maximum of eight in total. For example, many experimental papers will be characterized by more than one keyword in the Experimental Methods class of the Subject Index as well as by several keywords from the Materials Index. The keywords will be used as labels for the use in electronic navigation tools. Thus, careful attention to giving a correct, useful description of your work will generate more thorough use of your paper once it is published.

version of 1 May 1998

Subject Index

Theoretical methods, models and techniques

- ☐ Ab initio quantum chemical methods and calculations
- ☐ Atom-solid interactions, scattering, diffraction
- ☐ Atomistic dynamics
- ☐ Computer simulations
- ☐ Construction and use of effective interatomic interactions
- ☐ Density functional calculations
- ☐ Electron density, excitation spectra calculations
- ☐ Electron-solid interactions, scattering, diffraction
- ☐ Equilibrium thermodynamics and statistical mechanics
- ☐ Green's function methods
- ☐ Ion-solid interactions, scattering, channeling
- ☐ Ising models
- ☐ Jellium models
- ☐ Many body and quasi-particle theories
- ☐ Models of non-equilibrium phenomena
- ☐ Models of non-linear phenomena
- ☐ Models of surface chemical reactions
- ☐ Models of surface kinetics
- ☐ Molecular dynamics
- ☐ Monte Carlo simulations
- ☐ Non-equilibrium thermodynamics and statistical mechanics
- ☐ Semi-empirical models and model calculations

Experimental sample preparation and characterization methods

- ☐ Adsorption isotherms
- ☐ Appearance potential spectroscopy
- ☐ Atom-solid reactions
- ☐ Atom-solid scattering and diffraction - elastic
- ☐ Atom-solid scattering and diffraction - inelastic
- ☐ Atomic force microscopy (AFM)
- ☐ Auger electron spectroscopy (AES)
- ☐ Chemical vapor deposition
- ☐ Desorption induced by electronic

transitions (DIET)

- ☐ Angle resolved DIET
- ☐ Electron stimulated desorption (ESD)
- ☐ Photon stimulated desorption (PSD)
- ☐ Surface photochemistry
- ☐ Electrical transport measurements
- ☐ Electrochemical methods
- ☐ Electron emission measurements
- ☐ Exoelectron emission
- ☐ Field emission
- ☐ Photoemission
- ☐ Secondary electron emission
- ☐ Thermally-stimulated emission
- ☐ Electron energy loss spectroscopy (EELS)
- ☐ Electron microscopy
 - ☐ Ballistic electron emission microscopy (BEEM)
 - ☐ Low-energy electron microscopy (LEEM)
 - ☐ Reflection electron microscopy (REM)
 - ☐ Scanning electron microscopy (SEM)
 - ☐ Scanning transmission electron microscopy (STEM)
- ☐ Electron-solid diffraction
 - ☐ Auger electron diffraction
 - ☐ Low energy electron diffraction (LEED)
 - ☐ Photoelectron diffraction
 - ☐ Photoelectron holography
 - ☐ Reflection high-energy electron diffraction (RHEED)
 - ☐ Transmission high-energy electron diffraction
- ☐ Electron-solid scattering and transmission - elastic
- ☐ Electron-solid scattering and transmission - inelastic
- ☐ Electron spin resonance
- ☐ Ellipsometry
- ☐ Field emission microscopy
- ☐ Field emission spectroscopy
- ☐ Field ion microscopy

- ☐ Inverse photoemission spectroscopy
- ☐ Ion etching
- ☐ Ion implantation
- ☐ Ion scattering spectroscopy
 - ☐ High energy ion scattering (HEIS)
 - ☐ Low energy ion scattering (LEIS)
 - ☐ Medium energy ion scattering (MEIS)
- ☐ Isotopic exchange/traces
- ☐ Laser methods
 - ☐ Laser annealing
 - ☐ Laser induced thermal desorption (LITD)
 - ☐ Resonance enhanced multiphoton ionization mass spectroscopy (REMPI/MS)
- ☐ Liquid phase epitaxy
- ☐ Magnetic measurements
- ☐ Metastable induced electron spectroscopy (MIES)
- ☐ Molecular beam epitaxy (MBE)
- ☐ Molecule-solid reactions
- ☐ Molecule-solid scattering and diffraction - elastic
- ☐ Molecule-solid scattering and diffraction - inelastic
- ☐ Mössbauer spectroscopy
- ☐ Neutron scattering
- ☐ Non-linear optical methods
 - ☐ Second harmonic generation
 - ☐ Sum frequency generation
- ☐ Nuclear magnetic resonance
- ☐ Nuclear reaction analysis
- ☐ Photoelectron spectroscopy
 - ☐ Angle resolved photoemission
 - ☐ Soft X-ray photoelectron spectroscopy
 - ☐ Visible and ultraviolet photoelectron spectroscopy
 - ☐ X-ray photoelectron spectroscopy
- ☐ Synchrotron radiation photoelectron spectroscopy
- ☐ Photon absorption spectroscopy
 - ☐ Extended X-ray absorption fine structure (EXAFS)

- ☐ Infrared absorption spectroscopy
- ☐ Near edge extended X-ray absorption fine structure (NEXAFS)
- ☐ Photoacoustic spectroscopy
- ☐ Surface extended X-ray absorption fine structure (SEXAFS)
- ☐ Visible/ultraviolet absorption spectroscopy
- ☐ X-ray absorption spectroscopy
- ☐ Photon stimulated desorption
- ☐ Plasma processing
- ☐ Positron spectroscopy
- ☐ Radioactive tracer methods
- ☐ Raman scattering spectroscopy
- ☐ Reflection spectroscopy
- ☐ Scanning tunneling microscopy
- ☐ Scanning tunneling spectroscopies
- ☐ Secondary ion mass spectroscopy
- ☐ Solid phase epitaxy
- ☐ Sputter deposition
- ☐ Surface photovoltage spectroscopy
- ☐ Thermal desorption spectroscopy
- ☐ Work function measurements
- ☐ X-ray emission
- ☐ X-ray scattering, diffraction, and reflection
- ☐ X-ray standing waves

Phenomena

- ☐ Adhesion
- ☐ Adsorption kinetics
- ☐ Atom emission
- ☐ Atom-solid interactions
- ☐ Auger ejection
- ☐ Bending of surfaces
- ☐ Catalysis
- ☐ Chemisorption
- ☐ Compound formation
- ☐ Conductivity
- ☐ Corrosion
- ☐ Crystallization
- ☐ Dielectric phenomena
- ☐ Diffusion and migration
- ☐ Electrical transport (conductivity, resistivity, mobility etc.)
- ☐ Electron bombardment
- ☐ Electron emission
- ☐ Electron-solid interactions
- ☐ Electron stimulated desorption
- ☐ Energy dissipation
- ☐ Epitaxy
- ☐ Etching
- ☐ Evaporation and sublimation
- ☐ Faceting
- ☒ Field effect
- ☐ Field emission
- ☐ Field evaporation
- ☒ Field ionization
- ☐ Friction
- ☐ Growth
- ☐ Hall effect
- ☐ Interface states
- ☐ Ion bombardment
- ☐ Ion emission
- ☐ Ion implantation
- ☐ Ion-solid interactions
- ☐ Light scattering
- ☐ Lubrication
- ☐ Luminescence
 - ☐ Atom/ion *stimulated luminescence*
 - ☐ Chemiluminescence
 - ☐ Electroluminescence
 - ☐ Photoluminescence

- ☐ Magnetic phenomena (cyclotron resonance, phase transitions, etc.)
- ☐ Nucleation
- ☐ Oxidation
- ☐ Photochemistry
- ☐ Photoconductivity
- ☐ Photoelectron diffraction
- ☐ Photoelectron emission
- ☐ Photon emission
- ☐ Photon stimulated desorption
- ☐ Physical adsorption
- ☐ Piezoelectric effect
- ☐ Positron-solid interactions
- ☐ Quantum effects
- ☐ Radiation damage
- ☐ Second harmonic generation
- ☐ Secondary electron emission
- ☐ Self-assembly
- ☐ Sintering
- ☐ Sputtering
- ☐ Sticking
- ☐ Step formation and bunching
- ☐ Superconductivity
- ☒ Surface chemical reaction
- ☐ Surface diffusion
- ☐ Surface electrical transport (surface conductivity, surface recombination, etc.)
- ☐ Surface electronic phenomena (work function, surface potential, surface states, etc.)
- ☐ Surface energy
- ☐ Surface melting
- ☐ Surface photovoltage
- ☐ Surface relaxation and reconstruction
- ☐ Surface roughening
- ☐ Surface segregation
- ☐ Surface stress
- ☐ Surface structure, morphology, roughness, and topography
- ☐ Surface tension
- ☐ Surface thermodynamics (including phase transitions)
- ☐ Surface waves
 - ☐ Acoustic waves
 - ☐ Capillary waves
 - ☐ Magnons
 - ☐ Phonons
 - ☐ Plasmons
 - ☐ Polaritons
- ☐ Thermal desorption
- ☐ Thermionic emission
- ☐ Tribology
- ☐ Tunneling
- ☐ Vibrations of adsorbed molecules
- ☐ Wetting

Materials Index

ELEMENTAL AND CHEMICAL IDENTITY

(Include each component of an interface or multilayer structure as a separate category. Add your own specific elemental or chemical label is a suitable entry is not on the list.)

Elements

- ☐ Alkali metals
- ☐ Alkaline earth metals
- ☐ Aluminum
- ☐ Antimony
- ☐ Arsenic
- ☐ Bismuth
- ☐ Boron
- ☐ Bromine
- ☐ Cadmium
- ☐ Carbon
- ☐ Cerium
- ☐ Chalcogens
- ☐ Chlorine
- ☐ Chromium
- ☐ Cobalt
- ☐ Copper
- ☐ Diamond
- ☐ Gallium
- ☐ Germanium
- ☐ Gold
- ☐ Graphite
- ☐ Hafnium
- ☐ Hydrogen
- ☐ Indium
- ☐ Iodine
- ☐ Iridium
- ☐ Iron
- ☐ Lanthanides
- ☐ Lead
- ☐ Manganese
- ☐ Mercury
- ☐ Molybdenum
- ☐ Nickel
- ☐ Niobium
- ☐ Nitrogen
- ☐ Noble gases
- ☐ Osmium
- ☐ Palladium
- ☐ Phosphorus
- ☒ Platinum
- ☐ Rhenium
- ☐ Rhodium
- ☐ Ruthenium
- ☐ Scandium
- ☐ Silicon
- ☐ Silver
- ☐ Tantalum
- ☐ Technetium
- ☐ Thallium
- ☐ Thorium
- ☐ Tin
- ☐ Titanium
- ☐ Tungsten
- ☐ Uranium
- ☐ Vanadium
- ☐ Ytterbium
- ☐ Yttrium
- ☐ Zinc
- ☐ Zirconium
- ☐ Other elements*

Compounds (non-molecular solids)

- ☐ Alkali halides
- ☐ Alloys
- ☐ Aluminum oxide
- ☐ Barium oxide
- ☐ Biological compounds
- ☐ Borides
- ☐ Boron nitride
- ☐ Cadmium selenide
- ☐ Cadmium sulphide
- ☐ Cadmium telluride
- ☐ Carbides
- ☐ Cobalt oxides
- ☐ Copper oxides
- ☐ Gallium antimonide
- ☐ Gallium arsenide
- ☐ Gallium nitride
- ☐ Gallium phosphide
- ☐ Gallium selenide
- ☐ Halides
- ☐ Hydrides
- ☐ Indium antimonide
- ☐ Indium arsenide
- ☐ Indium oxides
- ☐ Indium phosphide
- ☐ Inorganic compounds
- ☐ Iron oxide
- ☐ Lead telluride
- ☐ Magnesium oxides
- ☐ Mercury telluride
- ☐ Mica
- ☐ Molybdenum oxides
- ☐ Nickel carbide
- ☐ Nickel oxides
- ☐ Nickel sulphide
- ☐ Nitrides
- ☐ Silicides
- ☐ Silicon carbide
- ☐ Silicon-germanium
- ☐ Silicon nitride
- ☐ Silicon oxides
- ☐ Steel
- ☐ Sulphides
- ☐ Tin oxides
- ☐ Tin telluride
- ☐ Titanium carbide
- ☐ Titanium oxide
- ☐ Tungsten oxide
- ☐ Uranium oxide
- ☐ Vanadium oxide
- ☐ Zeolites
- ☐ Zinc oxide
- ☐ Zinc selenide
- ☐ Other compounds

Molecules

- ☐ Alcohols
- ☐ Aldehydes
- ☐ Alkanes
- ☐ Alkenes
- ☐ Alkynes
- ☐ Ammonia
- ☐ Aromatics
- ☐ Biological molecules - nucleic acids
- ☐ Biological molecules - proteins
- ☐ Biological molecules - other
- ☐ Carbon dioxide
- ☐ Carbon monoxide
- ☐ Carboxylic acid
- ☐ Cyanogen
- ☐ Deuterium
- ☐ Esters
- ☐ Ethers

- ☐ Fullerenes
- ☐ Halogens
- ☐ Hydrogen
- ☐ Hydrogen cyanide
- ☐ Hydrogen sulphide
- ☐ Ketones
- ☐ Nitrogen
- ☐ Nitrogen oxides
- ☐ Oxygen
- ☐ Ozone
- ☐ Phosphine
- ☐ Silane
- ☐ Sulphur dioxide
- ☐ Sulphur hexafluoride
- ☒ Water
- ☐ Other molecules

PHYSICAL STATE**Surfaces**

- ☐ Amorphous surfaces
- ☐ Dendritic and/or fractile surfaces
- ☐ Glass surfaces
- ☐ Liquid surfaces
- ☐ Polycrystalline surfaces
- ☐ Single crystal surfaces
 - ☐ *Low index single crystal surfaces*
 - ☐ *High index single crystal surfaces*
 - ☐ *Stepped single crystal surfaces*
 - ☐ *Vicinal single crystal surfaces*
 - ☐ *Curved surfaces*
- ☐ Surface defects
- ☐ Whiskers

Interfaces

- ☐ Crystalline-amorphous interfaces
- ☐ Crystalline-glass interfaces
- ☐ Grain boundaries
- ☐ Liquid-gas interfaces
- ☐ Single crystal epitaxy
- ☐ Solid-liquid interfaces
- ☐ Solid-gas interfaces

Heterostructures

- ☐ Heterojunctions
- ☐ Quantum wells
- ☐ Superlattices

Non-epitaxial thin film structures

- ☒ Amorphous thin films
- ☐ Ceramic thin films
- ☐ Glassy thin films
- ☒ Polycrystalline thin films

☐ Adatoms☐ Clusters**Particulate composites**

- ☐ Blacks
- ☐ Ceramics
- ☐ Powders

☐ Coatings☐ Porous solids**ELECTRICAL AND MAGNETIC BEHAVIOR****Surfaces and/or films**

- ☐ Insulating films
- ☐ Insulating surfaces
- ☐ Magnetic films
- ☐ Magnetic surfaces
- ☐ Metallic films
- ☐ Metallic surfaces
- ☐ Semiconducting films
- ☐ Semiconducting surfaces
- ☐ Superconducting films
- ☐ Superconducting surfaces

Interfaces

- ☐ Magnetic interfaces
- ☐ Metal-electrolyte interfaces
- ☐ Metal-insulator interfaces
- ☐ Metal-metal interfaces
- ☐ Metal-semiconductor interfaces
- ☐ Schottky barrier
- ☐ Semiconductor-electrolyte interfaces
- ☐ Semiconductor-insulator interfaces
- ☐ Semiconductor-semiconductor interfaces
- ☐ Semiconductor-superconductor interfaces
- ☐ Other interfaces

Heterostructures and thin film structures

- ☐ Metal-metal magnetic heterostructures
- ☐ Metal-metal magnetic thin film structures
- ☐ Metal-metal nonmagnetic heterostructures
- ☐ Metal-metal nonmagnetic thin film structures
- ☐ Metal-oxide-semiconductor (MOS) structures
- ☐ Metal-semiconductor magnetic heterostructures
- ☐ Metal-semiconductor magnetic thin film structures
- ☐ Metal-semiconductor nonmagnetic heterostructures
- ☐ Metal-semiconductor nonmagnetic thin film structures
- ☐ Semiconductor-semiconductor heterostructures
- ☐ Semiconductor-semiconductor thin film structures
- ☐ Superconductor-semiconductor heterostructures
- ☐ Superconductor-semiconductor thin film structures
- ☐ Other heterostructures
- ☐ Other thin film structures

☐ Contacts

* Please, fill in necessary new Materials Index Keyword. If the new keyword is indicated on the manuscript, please make clear to which subcategory it belongs.

1. Introduction

Electrode/electrolyte interfaces typically support high surface electric fields on the order of 1-3 V/Å [1-3]. While the surface electric field depends upon electrode potential and the nature of electrode and electrolyte, the response of the electric field to these parameters and its subsequent influence in electrochemical processes remain unknown due to the difficulty of directly controlling the field. The field at the surface can be independently controlled through the use of sharp field emitter tips. Fields of up to 5 V/Å can be obtained by applying potentials of 1-5 kV onto tips of radius 100-1000 Å. Because the tips themselves are nanometer-sized objects, studies of this nature are also relevant for understanding the role of water in process nanotechnology.

Despite the significance of field effects on water at electrode/electrolyte interfaces [4], there have been only a few studies of its behavior in high electric fields. These studies found that hydrated protons $(\text{H}_2\text{O})_n\text{H}^+$, with n ranging from 1-10, desorb from water covered emitter tips [5-10]. Protonated water clusters are formed at applied fields as low as 0.15 V/Å [6, 7]. Most studies involved water deposited in the presence of an applied field, and as a result, the ordering of the water layer was strongly influenced by the electric field. Only the work of Stintz and Panitz studied the effects of electric fields on amorphous ice [9, 11]. They formed thin layers (100 Å) of amorphous ice by depositing water at cryogenic temperatures in the absence of an applied field. They also detected hydrated protons, with the predominant cluster size being three water molecules ($n = 3$). Stintz and Panitz found that ionization depends upon the morphology of the water layer: above the glass transition temperature larger water clusters form and the ionization field decreases less quickly with increasing temperature [9].

Multilayers of water can be deposited on cryogenic surfaces (< 160 K) under vacuum

conditions [12]. Water deposited under these conditions forms either amorphous ice, cubic ice, hexagonal ice, or a mixture thereof. Amorphous ice can be used to simulate room temperature water because it is a metastable form of liquid water [13]. This interpretation is supported by x-ray diffraction, neutron diffraction and Raman spectroscopy results [14-17]. Evaporation rate and calorimetry data have shown that thermodynamic continuity exists between amorphous ice and liquid water [18-21]. Above its glass transition temperature of 136 K, amorphous ice is believed to be a highly viscous, metastable liquid [22].

The structure of the water layer depends upon the surface temperature, deposition rate [13, 17, 23-26] and the wettability of the surface [27]. Amorphous ice forms as a consequence of the initial growth conditions and is not necessarily an inherent growth property of ice [27]; its formation is favored at deposition rates less than 10 \AA/s , low temperatures [13, 17, 23], and on surfaces more easily wetted by water [27]. The morphology of amorphous ice depends on deposition temperature. Amorphous ice deposited below 110 K is a porous solid with a large number of micropores that begin to collapse when the temperature of the sample is raised above 120 K [26]. Ice deposited between 110 and 140 K has a higher density because fewer micropores form in the layer [26]. Brown et. al. have determined that the density varies linearly from 0.79 g/cm^3 at 80 K to 0.93 g/cm^3 at 130 K. The density is constant above 130 K [12].

Crystallization of amorphous ice depends strongly on deposition conditions and thermal history [21, 25]. Pure amorphous ice crystallizes to cubic ice near 150 K [13, 22, 26-30]. There have been some reports that crystallization occurs between 130-140 K [24, 29, 31]. The lower crystallization temperature is attributed to the presence of crystalline nuclei in the sample [13, 17]. Crystalline nuclei will form if the water is deposited with a supersonic jet [9] and at higher

deposition temperatures. Amorphous ice deposited below 113 K contains only minute quantities of crystalline ice [32], but the crystalline content increases with increasing deposition temperature [25, 27]. The temperature dependence of the crystalline content of the water layer is not currently known, but there are reports that no more than 30% of the sample crystallizes to cubic ice before crystallization to hexagonal ice [31, 33]. The crystallization temperature of hexagonal ice is 200 K [28].

In this paper we report experimental results for field ionization of water. Water was adsorbed at temperatures of 100 to 150 K onto a platinum field emitter tip under field-free conditions in ultrahigh vacuum. Ionization was examined by isothermal ramped field desorption (RFD) performed as a function of temperature and water layer thickness. These experiments differed from those of Stintz and Panitz in that a wide range of water thicknesses was studied, thus allowing exploration of the thickness-dependence of ionization and determination of the surface field required to ionize water. We interpret the results in terms of the temperature and thickness dependence of the field at ionization onset. Comparison of the experimental results with those of a previous modeling study will be discussed elsewhere [34].

2. Equipment and Procedure

The experimental apparatus and procedure have been described previously [35] and will therefore be described only briefly. The vacuum chamber was pumped by a turbo-molecular pump and titanium getter pump to obtain a base pressure of 10^{-10} torr. A field emitter tip was used to generate electric fields as large as 4 V/Å. Ions produced by the tip were projected onto a pair of chevron microchannel plates (MCP) and directed onto a phosphor screen to form a greatly magnified, projection image of the tip surface. This image shows the detailed atomic

arrangements of the hemispherical tip surface [36]. Field ionization images were recorded with a CCD camera and VCR.

A platinum tip, oriented along the [100] axis, was spot-welded to a 0.25 mm diameter heating loop mounted to the bottom of a cryogenically cooled downtube. The temperature was measured by a chromel/alumel thermocouple spot-welded to the heating loop. The desired temperature was maintained within ± 0.3 K by a PID temperature controller connected to a d.c. power supply for resistive heating. A high voltage feedthrough at the bottom of the downtube provided high voltage isolation for the heating loop/tip assembly.

The field emitter tip was electrochemically etched from 0.013 mm diameter platinum wire at 2-3 V d.c. in a molten mixture of sodium chloride and sodium nitrate. The tip radius was determined from the best imaging field in neon of 3.75 V/Å [37]. The relationship between the applied potential V_t and the applied field F_{app} is

$$F_{app} = V_t / \beta r_t, \quad (1)$$

where β is the shape factor and r_t is the tip radius. The shape factor is 5 for a typical emitter tip [38]. The tip radius in these experiments ranged from 335 to 374 Å. Tip radii determined from the best imaging field were within 20% of those estimated by counting the number of lattice steps between the (001) and (113) planes in the field ionization images. The relative error in the electric fields reported in these experiments is less than 5%. In this paper the term “applied field” is used to describe the field that would occur at a bare tip surface in vacuum for a given applied tip potential.

A three-step procedure was used to ensure that the tip was free from contaminants at the beginning of each experimental run. First, the tip was heated to 500 K to desorb water from the tip and heating loop assembly. Second, any remaining contaminants were field desorbed from the tip by imaging in neon and hydrogen. Finally, a small amount of platinum was field desorbed in neon to ensure that the surface was atomically clean.

Prior to dosing, water was degassed with both liquid nitrogen and dry ice in several freeze-thaw cycles. Water was introduced into the background of the vacuum chamber through a variable leak valve to produce a uniform layer of ice on the tip under field-free conditions. The tip was held at the desired temperature during dosing. The tip was exposed to 5.0×10^{-7} torr of water for 2 to 60 minutes. The deposition rate was $\sim 0.8 \text{ \AA/s}$ under these conditions. Chamber pressures of less than 5.0×10^{-9} torr were typically achieved within 2 to 10 minutes after dosing. Water thicknesses of 50 to 3600 \AA were obtained from these exposures.

The water layer thickness was estimated from the empirical method developed by Brown et. al. [12]. The maximum growth rate of the water layer is determined by the incident flux J_{in} :

$$J_{in} = \frac{P_w}{N_w \sqrt{2\pi m k T_g}} \quad (2)$$

where P_w is the partial pressure of water, N_w the surface density of a monolayer of water, m the mass, k Boltzmann's constant, and T_g the gas temperature. The surface density of a monolayer of water is $1.056 \times 10^{15} \text{ molecules/cm}^2/\text{ML}$ [12]. It is necessary to correct the growth rate by the desorption flux J_{des} :

$$J_{des} = v_o \exp\left[\frac{-E_d}{kT_s}\right] \quad (3)$$

where v_o is the desorption pre-exponential factor of 4×10^{15} ML/s, E_d the desorption activation barrier of 48.25 kJ/mol [12], and T_s is the surface temperature. The condensation coefficient for the water layer is defined as:

$$\alpha = S(T) - \frac{J_{des}(T)}{J_{in}} \quad (4)$$

where $S(T)$ is the sticking coefficient. The sticking coefficient for water is 1.0 below 160 K [12]. The thickness of water on the surface is the difference between the amount of water deposited during deposition and the amount of water leaving the surface during chamber pump down:

$$t_w = \frac{M}{\rho N_A} \left(\frac{\alpha P_w}{\sqrt{2\pi m k T_g}} \tau_{exp} - J_{des} N_w \tau_{pump} \right) \quad (5)$$

where M is the molecular weight, ρ the density of the water adlayer, N_A Avagadro's number, τ_{exp} the exposure time, and τ_{pump} the pump down time. The second term in Eqn. 5 is very small at temperatures less than 145 K. The density of the water layer varies linearly from 0.8 g/cm³ at 80 K to 0.93 g/cm³ at 130 K [12].

Ramped field desorption (RFD) spectra were obtained after removing water from the background gas [11]. During the RFD runs, the potential applied to the tip was increased at a

rate of 10 V/s. When the field becomes sufficiently large, ions are created, desorb from the water layer, accelerate away from the tip radially, and are detected at the MCP/phosphor screen assembly. The signal from the phosphor screen was monitored by two rate meters, each with a time constant of 0.1 s. The first rate meter was always set to a sensitivity of 300 counts per second (CPS) full scale, while the second was adjusted to capture the entire peak. It was necessary to use a constant setting on the first rate meter to define an instrumental constant, which will be used later.

3. Results

The effects of temperature and ice thickness on water ionization were observed. In these experiments, the ice thickness was systematically varied at constant temperature. Data were collected at temperatures between 100 and 150 K. The ionization behavior for thin and thick layers and the effect of thickness on onset ionization are discussed below.

3.1. Ionization in Thin Layers

A CCD camera and VCR recorded the images on the phosphor screen during the field ramp. Ionization is indicated by bright dots in the field ionization images. In thin layers, ionization is randomly distributed on the tip surface. Fig. 1 shows an ionization image for a thin layer ($x = 0.7$) at 108 K, where

$$x = t_w / r_t. \quad (6)$$

This image is a typical frame from the video of the desorption event. At temperatures above 130

K, the bright dots are more localized, but they still have a very short duration, as shown in Fig. 2 for 133 K. The bright region in Fig. 2 was present in only one frame of the videotape.

The ramped field desorption spectra provide further insight into ionization of thin water layers. Fig. 3 shows a series of spectra obtained at varying temperatures at a dimensionless thickness of $x = 0.3 - 0.4$. As expected, the peaks shift to lower applied fields as temperature increases. At 103 K ionization occurs in a single peak. As temperature increases, the peaks begin to have multiple features. Above 130 K, these features split into two distinct peaks. The distance between the two peaks increases with increasing temperature because the location of the first peak is more strongly dependent upon temperature than the second peak.

3.2. Ionization in Thick Layers

The field ionization images for thick layers are also temperature dependent. Fig. 4 shows a typical ionization image sequence for temperatures below 130 K. At ionization onset the bright dots (ions) are randomly distributed. Fig. 4a shows the image at 108 K for a dimensionless thickness x of 4 at an applied field of 1.1 V/\AA . The number of dots gradually increases with applied field (Fig. 4b) until a critical field is reached and there is a bright flash, as shown in Fig. 4c. The bright flash has a short duration (approximately 1 second). After the flash, the screen is dark, indicating the absence of ionization. For very thick layers, there may be subsequent flashes as the field increases. These flashes may be ionization of water that has diffused to the tip from the shank.

The ionization images of thick layers above 130 K are quite different from the images at lower temperatures. Above 130 K ionization is confined to highly localized regions, or zones, which persist throughout ionization. A typical sequence above 130 K is shown in Fig. 5. This

sequence is for a dimensionless thickness x of 6 at 133 K. At ionization onset, the ionization zones are merely faint regions that grow in size and intensity as the applied field increases. Fig. 5a shows the field ionization image at an applied field of 1 V/\AA . The zones are relatively immobile and move only to distance themselves from neighboring ionization zones. This results in an approximately hexagonal pattern, as shown in Fig. 5b. As the field increases, the ionization zones increase in number and decrease in diameter. Eventually the zones become mobile and begin to move randomly on the surface as the applied field continues to increase. Near the end of ionization a dark region appears at the tip apex (Fig. 5c), which indicates the absence of ionization. The image in Fig. 5c shows that the dark region originates at the tip apex, but it can form at other locations. The ionization zones do not disappear, but retreat with the water layer as the dark region at the tip apex increases in size. As shown in Fig. 5.6c, occasionally some ionization continues in the dark region. This may indicate that not all water is removed from the tip apex or that water readsorbs onto the tip surface.

The differences in the ionization images above and below 130 K are reflected by the RFD spectra. Fig. 6 shows the effect of temperature on RFD spectra for water layers approximately ten times as thick ($x = 3$) as the water layers in Fig. 3. All peaks have a gradual onset as the applied field increases. The sharp spikes in the spectra below 130 K correspond to the flashes seen in the field ionization images. Above 130 K, the end of ionization is more gradual. Note that the area under the peaks in Fig. 6 is not constant. This may be due to changes in the size of the protonated water clusters with temperature.

3.3. Ionization Onset

The onset field of ionization $F_{app,o}$, defined experimentally as the applied field at which

ionization reaches 10 counts/s, was measured as a function of ice thickness. The ionization threshold of 10 counts/s is lower than used previously [35] due to the much better signal to noise ratio of these experiments. Fig. 7 shows the dependence of the onset field on thickness at 133 K. The data fall on two lines with a slope break at $x = 1.0$. This change of slope was present at all temperatures examined, though not at the same thickness or applied field.

The field ionization images and spectra show that ionization in thin layers differs from that in thick layers. The slope break in plots of ionization onset $F_{app,o}$ as a function of thickness x indicate that there may be a change in ionization mechanism with water layer thickness. In this study, thin layers are defined as points that fall below the change in slope (slope break) and thick layers as those that lie above the slope break. The dimensionless thickness x at the slope break, shown in Fig. 8, falls gradually from 2.3 near 100 K to 1.7 near 130 K. At 130 K, the dimensionless thickness at the slope break drops abruptly to 1.0 and then gradually decreases to 0.5 at 148 K.

The slopes $dF_{app,o}/dx$ above and below the slope break are strongly dependent upon temperature. Fig. 9 shows the temperature dependence of $dF_{app,o}/dx$ below the slope break (i.e., thin layers). Below 130 K, $dF_{app,o}/dx$ is approximately 0.1 V/Å and above 130 K it is approximately 0.3 V/Å. The slopes and error bars were calculated by linear regression of the data.

Fig. 10 shows the temperature dependence of $dF_{app,o}/dx$ above the slope break (i.e., thick layers). The slope steadily decreases from a value of approximately 0.1 V/Å near 100 K to 0.04 V/Å at 130 K. These values are of the same order of magnitude as the slopes of thin layers below 130 K. Above 130 K, $dF_{app,o}/dx$ for thick layers increases linearly with increasing

temperature as shown in Fig. 10. The values of $dF_{app,o}/dx$ for thick layers are an order of magnitude lower than for thin layers above 130 K.

Extrapolation of the thin coverage line in Fig. 7 to zero thickness gives an estimate of the actual field required to ionize the ice, F_o . Extrapolation is necessary to correct for screening of the field by water layers of finite thickness. The onset field F_o is a true, rather than applied, field because the influence of water layer thickness has been removed. The extrapolated onset fields are shown Fig. 11. The onset field abruptly changes to a lower field at 130 K. The trend in the extrapolated onset field is linear above and below 130 K.

4. Discussion

4.1. Phase Transition

The RFD data indicate that the properties of ice deposited on field emitter tips undergo a step change at 130 K. Evidence of this step change include:

- 1) differences in the ionization images for thin layers below 130 K (Fig. 1) and above 130 K (Fig. 2);
- 2) presence of ionization "zones" above 130 K (Fig. 5), but not below 130 K (Fig. 4), in the field ionization images of thick layers;
- 3) spikes in the RFD desorption spectra for thick layers below 130 K, but not above 130 K (Fig. 6);
- 4) change in the thickness at the slope break at 130 K (Fig. 8);

- 5) abrupt change in the RFD slopes of the thin and thick coverage lines at 130 K (Figs. 9-10); and
- 6) sudden decrease in the onset field at zero thickness at 130 K (Fig. 11).

Thus, not only the RFD spectra, but the ionization images indicate that the properties of the water layer undergo a step change at 130 K.

There is also evidence that the properties of the water layer depend upon the temperature at which the water is deposited. Preliminary data show that water layers ($x = 0.56$) desorbed below 145 K require lower ionization fields if they are deposited at 145 K, rather than at the desorption temperature. For example, water deposited and desorbed at 110 K has an ionization onset field of 0.57 V/\AA while water deposited at 145 K and desorbed at 110 K has an ionization onset field of 0.44 V/\AA . The onset fields for the data deposited at 145 K are more consistent with the higher temperature data in Fig. 11 than the lower temperature (i.e., the dashed line rather than the solid line). More data are required to make a definitive statement because this data was only collected at one thickness and, as a result, there is insufficient data to determine the onset field at zero thickness.

The step change in the ionization images, the thickness at the slope break, the RFD slopes for thin and thick layers, and the onset field at 130 K are indicative of a phase change. While our technique cannot identify the phases directly, the most likely phase change is from amorphous to crystalline ice [28]. The phase change in the RFD experiments occurs at 130 K, which is about 20 K lower than the crystallization temperature of pure amorphous ice [13, 22, 26-30].

The lower crystallization temperature for the RFD experiments is not unexpected. It is known that amorphous ice deposited above 113 K contains some crystalline ice [32] and that the

crystalline content increases with increasing deposition temperature [25, 27]. At the temperatures used in this study, crystalline nuclei should have been present in most of the deposited layers [24, 29, 31]. The presence of the crystalline nuclei lowers the crystallization temperature to 130-140 K [13, 17]. However, the electric fields in the RFD experiments are large and their effect should not be overlooked. Molecular dynamics simulations have shown that liquid water undergoes an abrupt phase transition to a cubic ice-like structure in the presence of a strong electric field (0.5 – 3 V/Å) [39-43]. Thus, both the high deposition temperatures and the electric field in the RFD experiments may have contributed to the lowering of the crystallization temperature. The effects of deposition temperature can be deconvoluted from field effects in future experiments by depositing the water layers at a set temperature and performing the RFD experiment at the desired temperature.

4.2. Temperature Dependence

The temperature dependence of the onset field of ionization provides information about the energetics of the ionization event. As discussed previously [35], the rate of thermally excited ionization may be written as:

$$r_{ion} = n_w v \exp \left[\frac{V_1 F_o + H_a - (\Delta P) F_o}{kT} \right], \quad (7)$$

where n_w is the areal density of water, v the pre-exponential factor, V_1 the field dependence of the potential of curve crossing between the neutral and ionic potential energy curves, F_o the onset field, H_a the field-free activation barrier, ΔP the difference between the dipole moment of the final

and initial states, k Boltzmann's constant, and T temperature. This expression assumes that the neutral and ionic potential energy curves are straight in the region of crossing and that terms due to the polarizability of water are small.

As a constant detection rate was used to determine the onset of ionization, an instrumental constant I_c can be estimated from Eqn. 7:

$$I_c = -\ln \left[\frac{r_{ion,o}}{n_w v} \right] = \frac{V_1 F_o + H_a - (\Delta P) F_o}{kT}, \quad (8)$$

where $r_{ion,o}$ is derived from the specified detection rate of 10 counts/s and the hemispherical area of the tip. The quantity in square brackets in Eqn. 7 is assumed to be independent of field. The instrumental constant is 45 for the specified detection rate and a tip radius of 350 Å [35]. Solving for F_o gives

$$F_o = \frac{1}{V_1 - (\Delta P)} (H_a - I_c kT). \quad (9)$$

This expression predicts a linear relationship between the onset field for ionization and the temperature. As shown in Fig. 11 our data fit two lines: one for the crystalline phase and one for the amorphous phase. The linear relationship for the amorphous phase is in excellent agreement with results for amorphous ice reported by Stintz and Panitz [9].

Extrapolation of the data to zero field provides an estimate of the field free activation barrier. The extrapolated temperatures for the amorphous and crystalline phases in Fig. 11 are

213 K and 216 K, respectively. Thus, the field-free activation barrier for ionization is 0.73 ± 0.03 eV for the amorphous phase and 0.7 ± 0.1 eV in the crystalline phase. This compares well with results from d.c. conductivity experiments for water between platinum electrodes which show that 0.74 eV is required to form a pair of ions from two solvated water molecules [44]. The error in the field-free activation energy is large for the crystalline phase because the data were taken over a relatively narrow temperature range and they have large error bars. It may be possible to obtain a better estimate of the field-free activation energy for the crystalline phase by extending the temperature range. This can be done by depositing crystalline ice at temperatures above 145 K [45, 46] and performing the RFD at lower temperatures.

Eqn. 9 indicates that the step change at 130 K in Fig. 11 could be due to a difference in the dipole moment between the two phases. If V_I is negligible [35] then the slope of $-0.004754 \text{ V \AA}^{-1} \text{ K}^{-1}$ for the amorphous phase is equivalent to a dipole moment of -3.9 Debye and the slope of $-0.003614 \text{ V \AA}^{-1} \text{ K}^{-1}$ in the crystalline phase is equivalent to a dipole moment of -5.1 Debye. If the final state hydronium ion is assumed to have a small dipole moment ($P_f \approx 0$), then this result gives values of 3.9 and 5.1 Debye for the initial state water molecules in amorphous and crystalline ice, respectively. The dipole moment of liquid water has been calculated to be $2.4 - 3.0$ Debye and that of hexagonal ice is predicted to be 3.1 Debye [47]. A likely explanation for the differences between the experimental and calculated values is that V_I is not zero. Unfortunately, the relative importance of the curve crossing (V_I) and the dipolar interaction effects (ΔP) cannot be measured with this method, and further research is necessary to devise a means for measuring these quantities independently.

5. Conclusions

Field ionization of water layers adsorbed under field-free conditions on a platinum tip occurs at field of 0.5 to 0.2 V/Å over a temperature range of 100 to 150 K. Ice deposited on field emitter tips undergoes a phase transition from amorphous to crystalline ice at 130 K, which is 20 K lower than the crystallization temperature of pure amorphous ice. The formation of crystalline nuclei in the ice and the presence of an applied field have been cited as contributors to the decrease in crystallization temperature. The data also show that the phase change is abrupt.

The field-free ionization activation barriers for both phases are in excellent agreement with the 0.74 eV required to form a pair of ions from a pair of solvated water molecules. At 130 K, there is a drop in the field required to ionize very thin water layers. This difference has been attributed to differences in dipole moments in the amorphous and crystalline phases. The estimated dipole moments for amorphous and crystalline ice are 3.9 Debye and 5.1 Debye, respectively. Further experiments are planned to reduce the errors in the field-free activation barrier and dipole moment estimates for the crystalline phase.

Acknowledgements

We gratefully acknowledge support of this work from the Office of Naval Research.

References

1. W. Schmickler, *Surf. Sci.* 335 (1995) 416.
2. D. Price and J. W. Halley, *J. Electroanal. Chem.* 159 (1983) 347.
3. J. Kreuzer, *Surf. Sci.* 246 (1991) 336.
4. D. L. Cocke and J. H. Block, *Surf. Sci.* 70 (1978) 363.
5. A. R. Anway, *J. Chem. Phys.* 50 (1969) 2012.
6. H. D. Beckey, *Z. Naturforschg* 14a (1959) 712.
7. H. D. Beckey, *Z. Naturforschg* 15a (1960) 822.
8. M. G. Inghram and R. Gomer, *Z. Naturforsch.* 10a (1955) 863.
9. A. Stintz and J. A. Panitz, *Surf. Sci.* 296 (1993) 75.
10. W. A. Schmidt, *Z. Naturforsch.* 19a (1964) 318.
11. A. Stintz and J. A. Panitz, *J. Appl. Phys.* 72 (1992) 741.
12. D. E. Brown, S. M. George, C. Huang, E. K. L. Wong, K. B. Rider, R. S. Smith, and B. D. Kay, *J. Phys. Chem.* 100 (1996) 4988.
13. D. S. Olander and S. A. Rice, *Proc. Nat. Acad. Sci. USA* 69 (1972) 98.
14. J. Wenzel, C. Linderstrom-Lang, and S. A. Rice, *Science* 187 (1975) 428.
15. C. G. Venkatesh, S. A. Rice, and A. H. Narten, *Science* 187 (1974) 927.
16. C. G. Venkatesh, S. A. Rice, and J. B. Bates, *J. Chem. Phys.* 63 (1975) 1065.
17. A. H. Narten, C. G. Venkatesh, and S. A. Rice, *J. Chem. Phys.* 64 (1976) 1106.
18. R. S. Smith and B. D. Kay, *Surf. Rev. Letters* 4 (1997) 781.
19. G. P. Johari, A. Hallbrucker, and E. Mayer, *Nature* 330 (1987) 552.
20. G. P. Johari, G. Fleissner, A. Hallbrucker, and E. Mayer, *J. Phys. Chem.* 98 (1994) 4719.

21. W. Hage, A. Hallbrucker, E. Mayer, and G. P. Johari, *J. Chem. Phys.* 100 (1994) 2743.
22. G. P. Johari, A. Hallbrucker, and E. Mayer, *J. Chem. Phys.* 92 (1990) 6742.
23. T. C. Sivakumar, S. A. Rice, and M. G. Sceats, *J. Chem. Phys.* 69 (1978) 3468.
24. W. Hagen, A. G. G. M. Tielens, and J. M. Greenberg, *Chem. Phys.* 56 (1981) 367.
25. N. J. Sack and R. A. Baragiola, *Phys. Rev. B* 48 (1993) 9973.
26. W. C. Simpson, M. T. Sieger, T. M. Orlando, L. Parenteau, K. Nagesha, and L. Sanche, *J. Chem. Phys.* 107 (1997) 8668.
27. P. Lofgren, P. Ahlstrom, D. V. Chakarov, J. Lausmaa, and B. Kasemo, *Surf. Sci.* 367 (1996) L19.
28. L. Onsager, D. L. Staebler, and S. Mascarenhas, *J. Chem. Phys.* 68 (1978) 3823.
29. A. Kouchi, *J. Cryst. Growth* 99 (1990).
30. P. Jenniskens and D. F. Blake, *Science* 265 (1994) 753.
31. P. Jenniskens, S. F. Banham, D. F. Blake, and M. R. S. McCoustra, *J. Chem. Phys.* 107 (1997) 1232.
32. E. Mayer and R. Pletzer, *Nature* 319 (1986) 298.
33. L. G. Dowell and A. P. Rinfret, *Nature* 188 (1960) 1144.
34. D. L. Scovell, *J. Chem. Phys.*, submitted.
35. T. D. Pinkerton, D. L. Scovell, A. L. Johnson, B. Xia, V. K. Medvedev, and E. M. Stuve, *Langmuir* 15 (1999) 851.
36. T. Sakurai, A. Sakai, and H. W. Pickering, *Atom-Probe Field Ion Microscopy and its Applications* (Academic Press, Inc., Boston, 1989).

37. T. T. Tsong, Atom-Probe Field Ion Microscopy (Cambridge University Press, Cambridge, 1990).
38. R. Gomer, Field Emission and Field Ionization (Harvard University Press, Cambridge, 1961).
39. G. Sutmann, J. Electroanal. Chem. 450 (1998) 289.
40. I. M. Svishchev and P. G. Kusalik, Phys. Rev. Letters 73 (1994) 975.
41. M. Watanabe, A. M. Brodsky, and W. P. Reinhardt, J. Phys. Chem. 95 (1991) 4593.
42. I. C. Yeh and M. L. Berkowitz, J. Electroanal. Chem. 450 (1998) 313.
43. X. Xia, L. Perera, U. Essmann, and M. L. Berkowitz, Surf. Sci. 335 (1995) 401.
44. P. V. Hobbs, Ice Physics (Clarendon Press, Oxford, 1974).
45. R. S. Smith, C. Huang, E. K. L. Wong, and B. D. Kay, Surf. Sci. 367 (1996) L13.
46. N. Materer, U. Starke, A. Barbieri, M. A. V. Hove, G. A. Somorjai, G. J. Kroes, and C. Minot, Surf. Sci. 381 (1997) 190.
47. E. R. Batista, S. S. Xantheas, and H. Jonsson, J. Chem. Phys. 109 (1998) 4546.

Captions

- Fig. 1. Field ionization image for a thin layer ($x = 0.7$) of water at 108 K, where x is the dimensionless thickness. The image is one frame from the video.
- Fig. 2. Field ionization image for a thin layer ($x = 0.7$) of water at 133 K. The image is one frame from the video.
- Fig. 3. Ramped field desorption spectra (total ion intensity) of water layers of thickness $x = 0.3 - 0.4$ as a function of temperature. Adsorption and desorption of water occurred at the indicated temperature.
- Fig. 4. Field ionization image sequence for a thick layer ($x = 4$) of water at 108 K: (a) Image at $F_{app} = 1.1 \text{ V/\AA}$; (b) $F_{app} = 1.3 \text{ V/\AA}$; (c) $F_{app} = 1.4 \text{ V/\AA}$.
- Fig. 5. Field ionization image sequence for a thick layer ($x = 6$) of water at 133 K. (a) $F_{app} = 1 \text{ V/\AA}$; ionization zones are stationary and persistent. (b) $F_{app} = 1.2 \text{ V/\AA}$; ionization zones have increased in number and are beginning to become mobile. (c) $F_{app} = 1.4 \text{ V/\AA}$, near the end of ionization; no ionization occurs in the dark region at the apex of the tip.
- Fig. 6. Ramped field desorption spectra (total ion intensity) of water layers of thickness $x = 2.7 - 3.3$ as a function of temperature.
- Fig. 7. Applied field at ionization onset as a function of deposited ice thickness, x , at 133 K.
- Fig. 8. Dimensionless thickness x at the slope break as a function of temperature.
- Fig. 9. Dependence on temperature T of $dF_{app,o}/dx$ for thin layers (i.e., below the slope break), where F_o is the applied field at ionization onset and x the dimensionless thickness.
- Fig. 10. Dependence on temperature T of $dF_{app,o}/dx$ for thick layers (i.e., above the slope break).

Fig. 11. Applied field at ionization onset F_o as a function of temperature T in the limit of zero coverage.

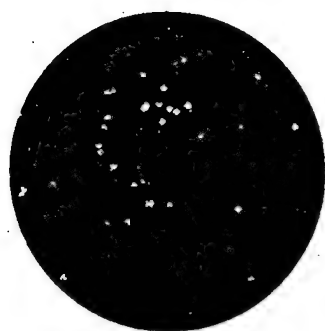


Fig. 1
Scovell et. al.

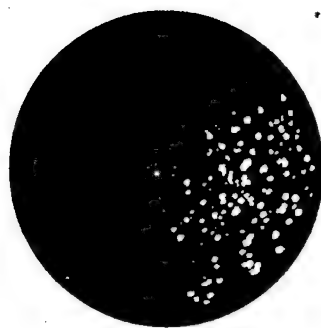


Fig. 2
Scovell et. al.

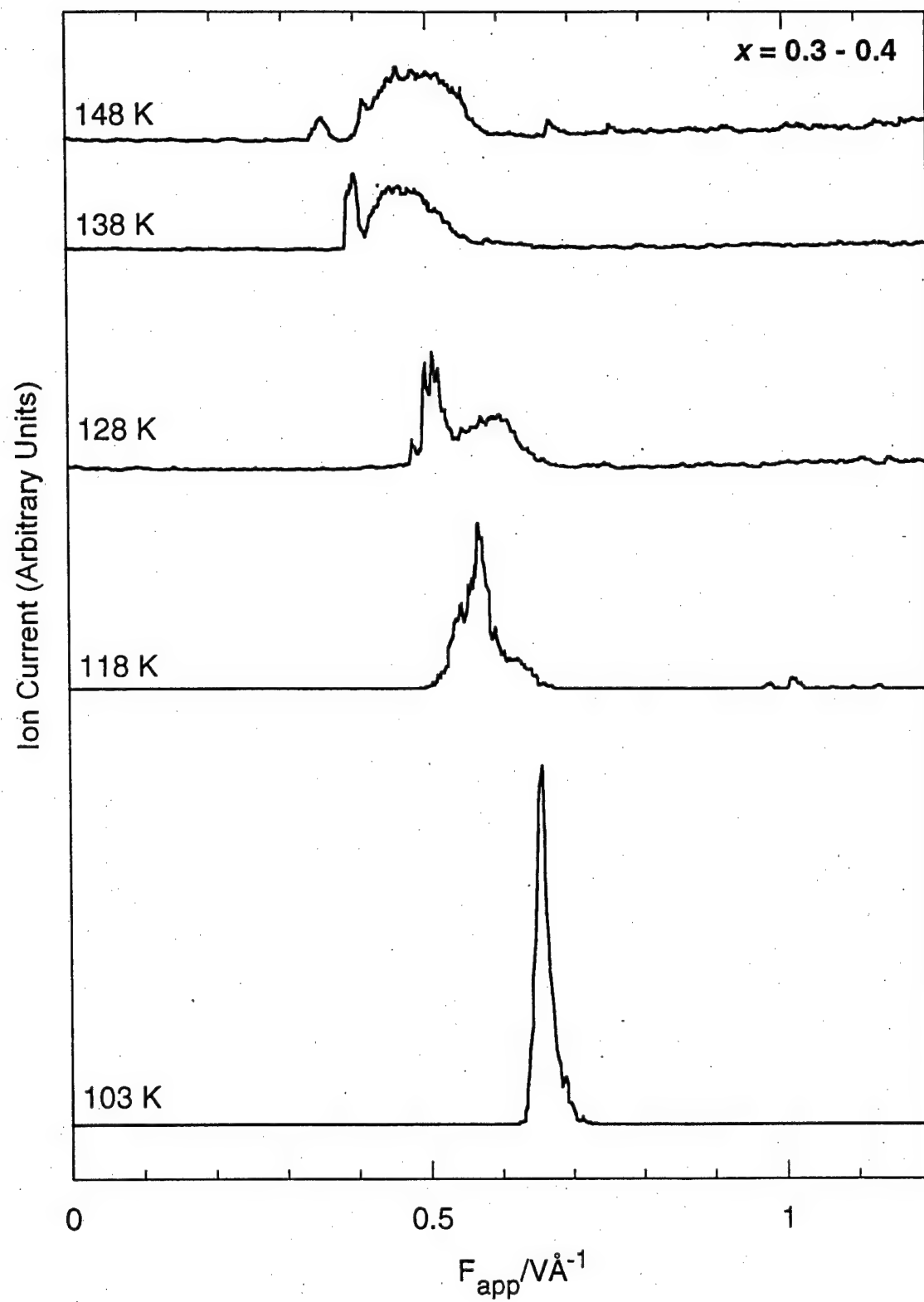


Fig. 3
Scovell et. al.

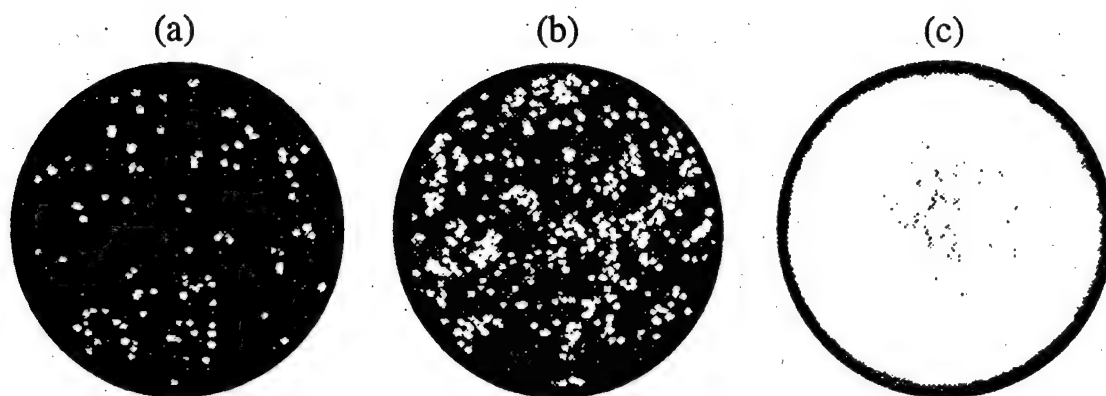


Fig. 4
Scovell et. al.

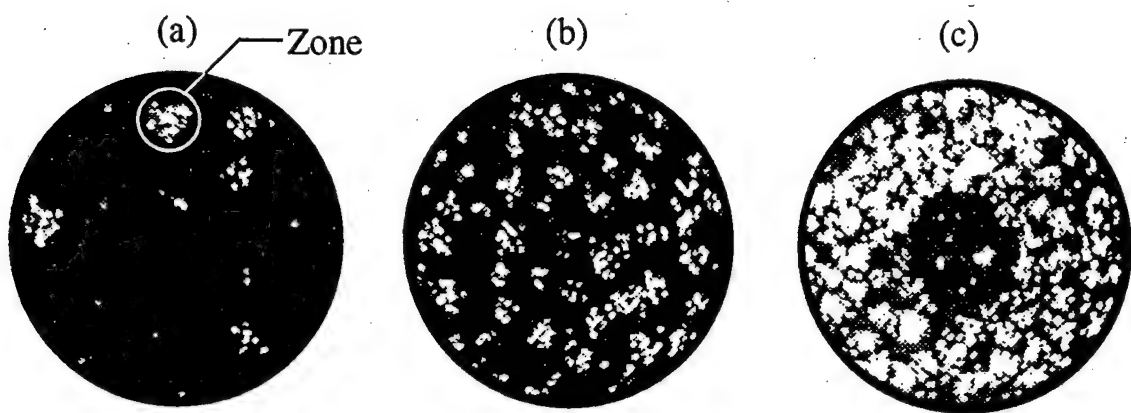


Fig. 5

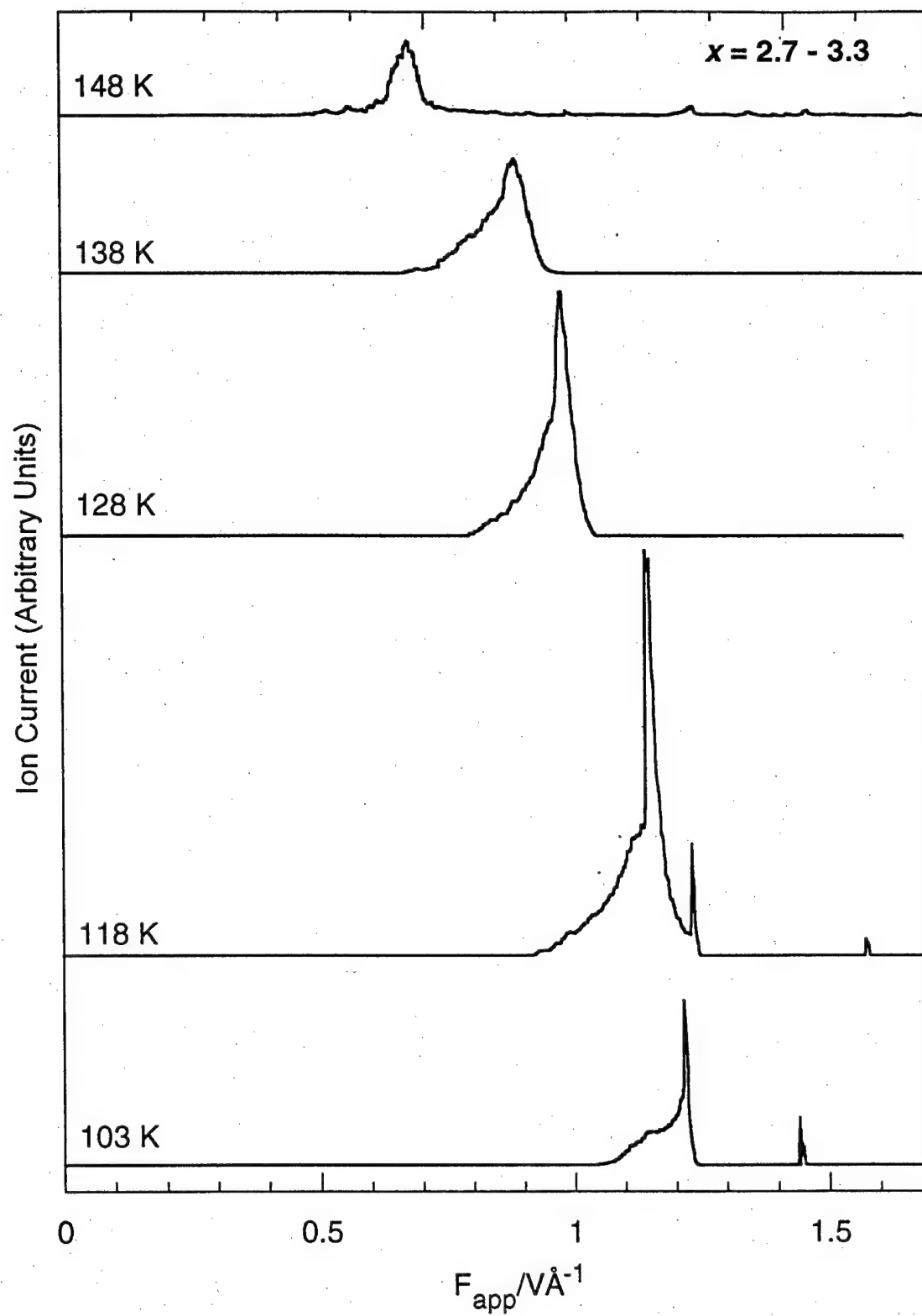


Fig. 6
Scovell et. al.

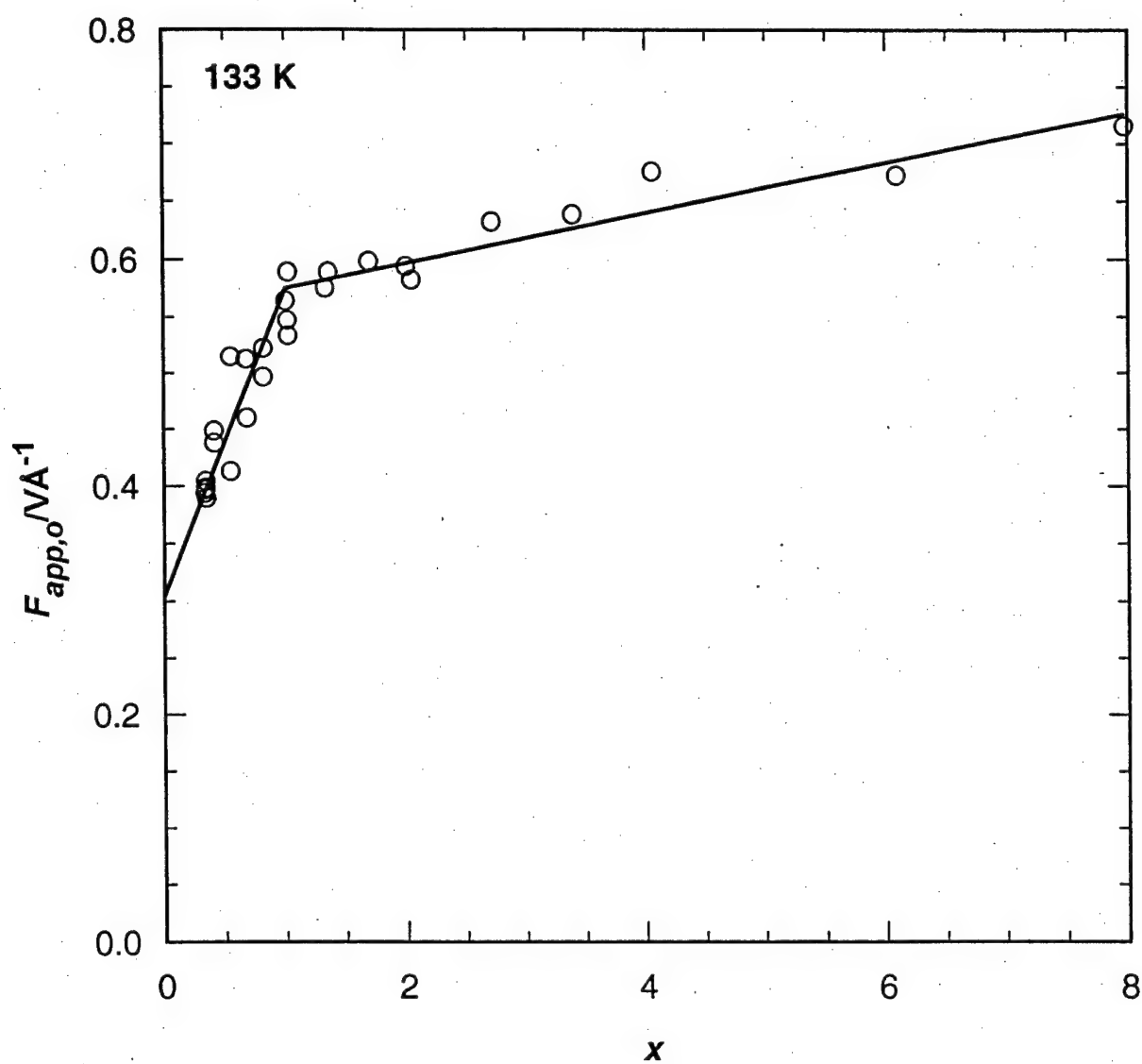


Fig.7
Scovell et. al.

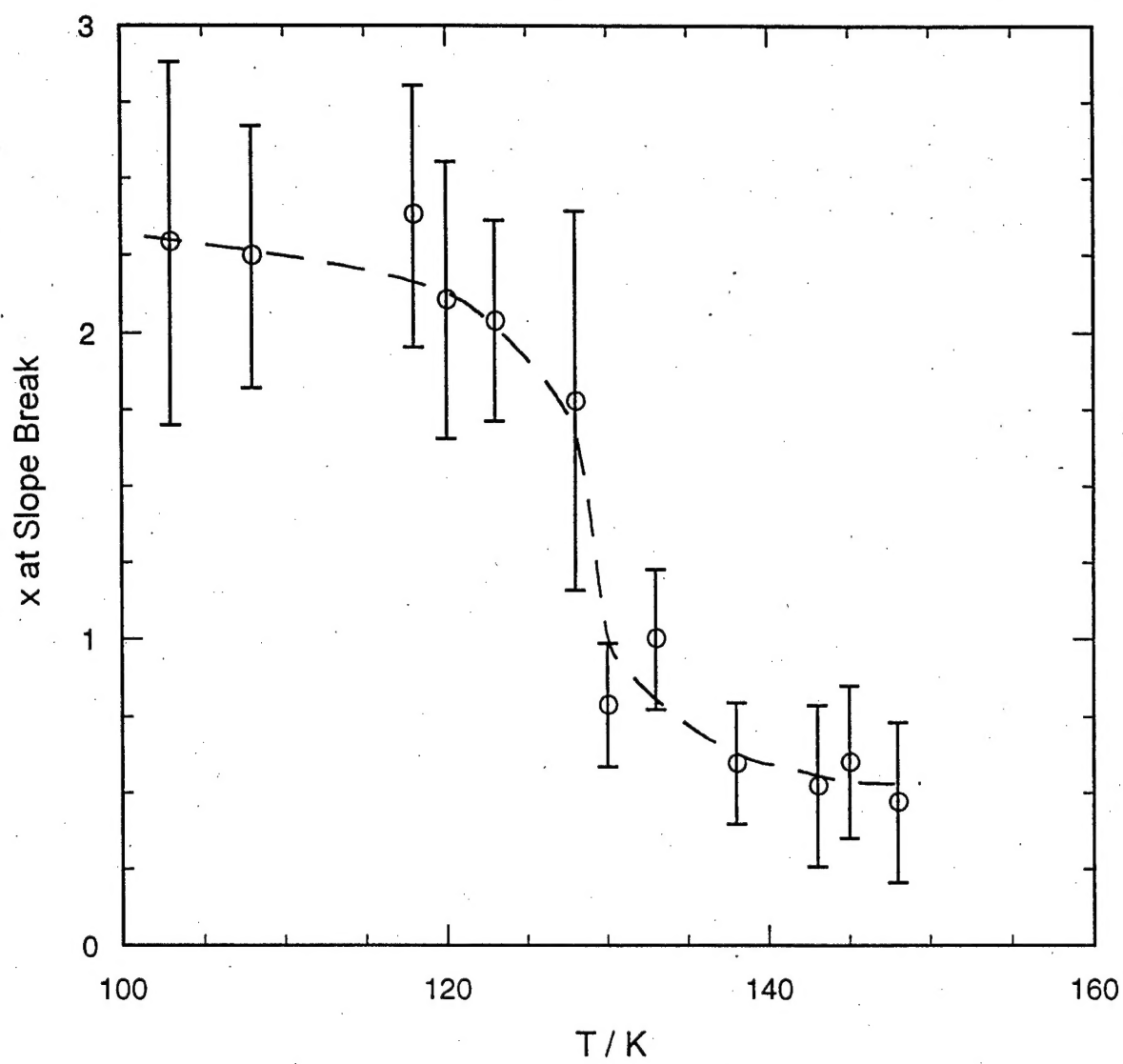


Fig. 8
Scovell et. al.

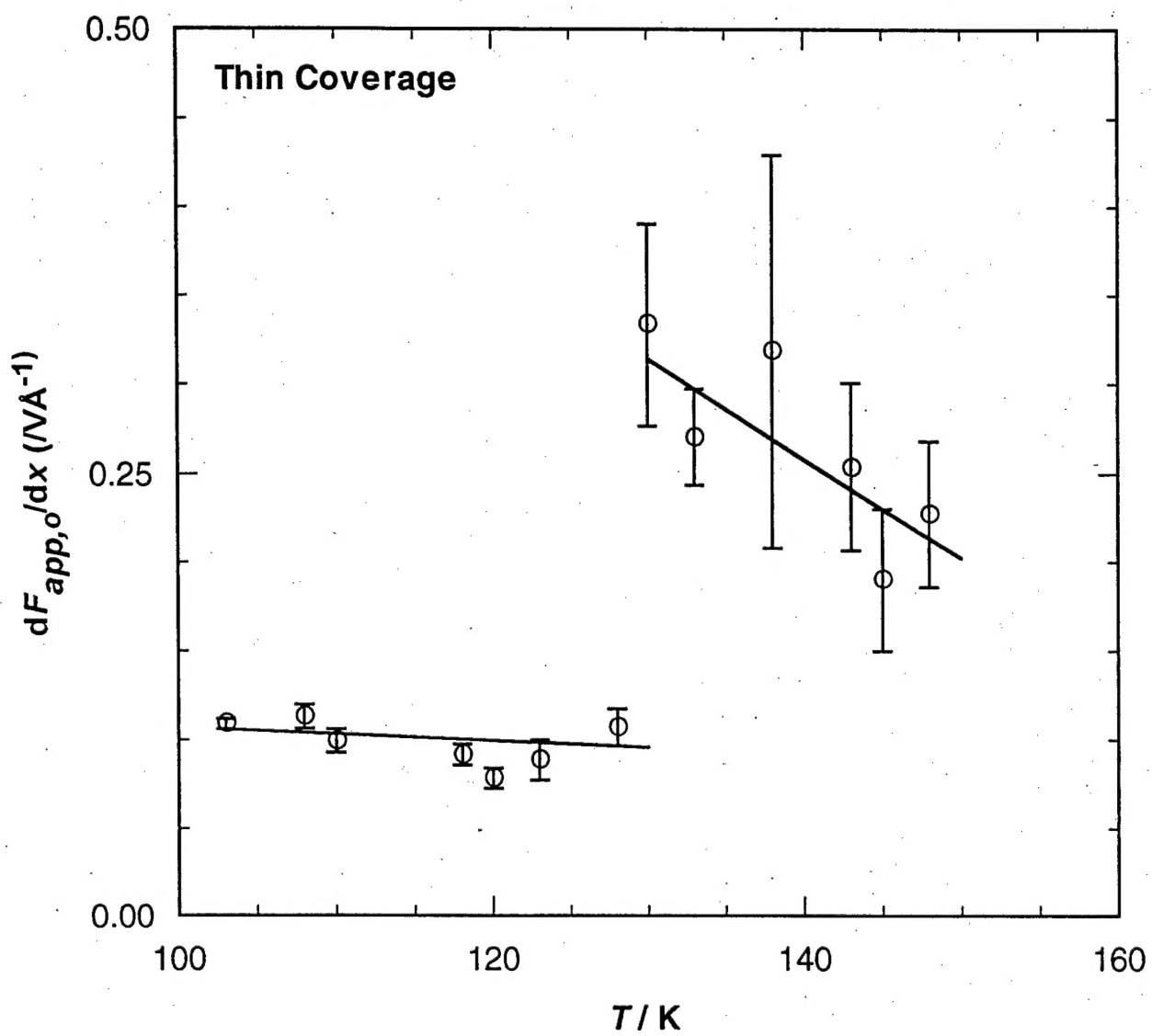


Fig. 9
Scovell et. al.

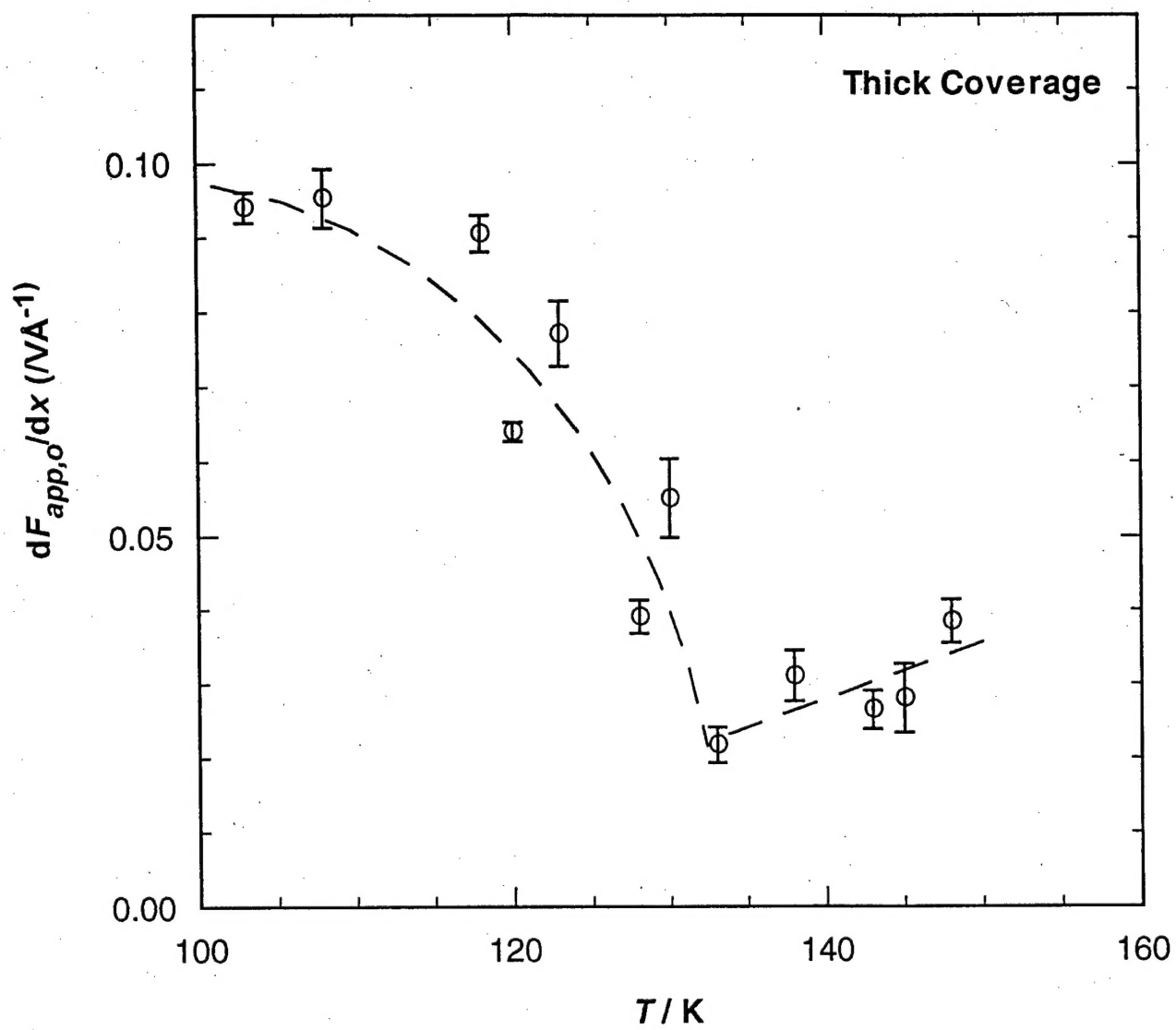


Fig. 10
Scovell et. al.

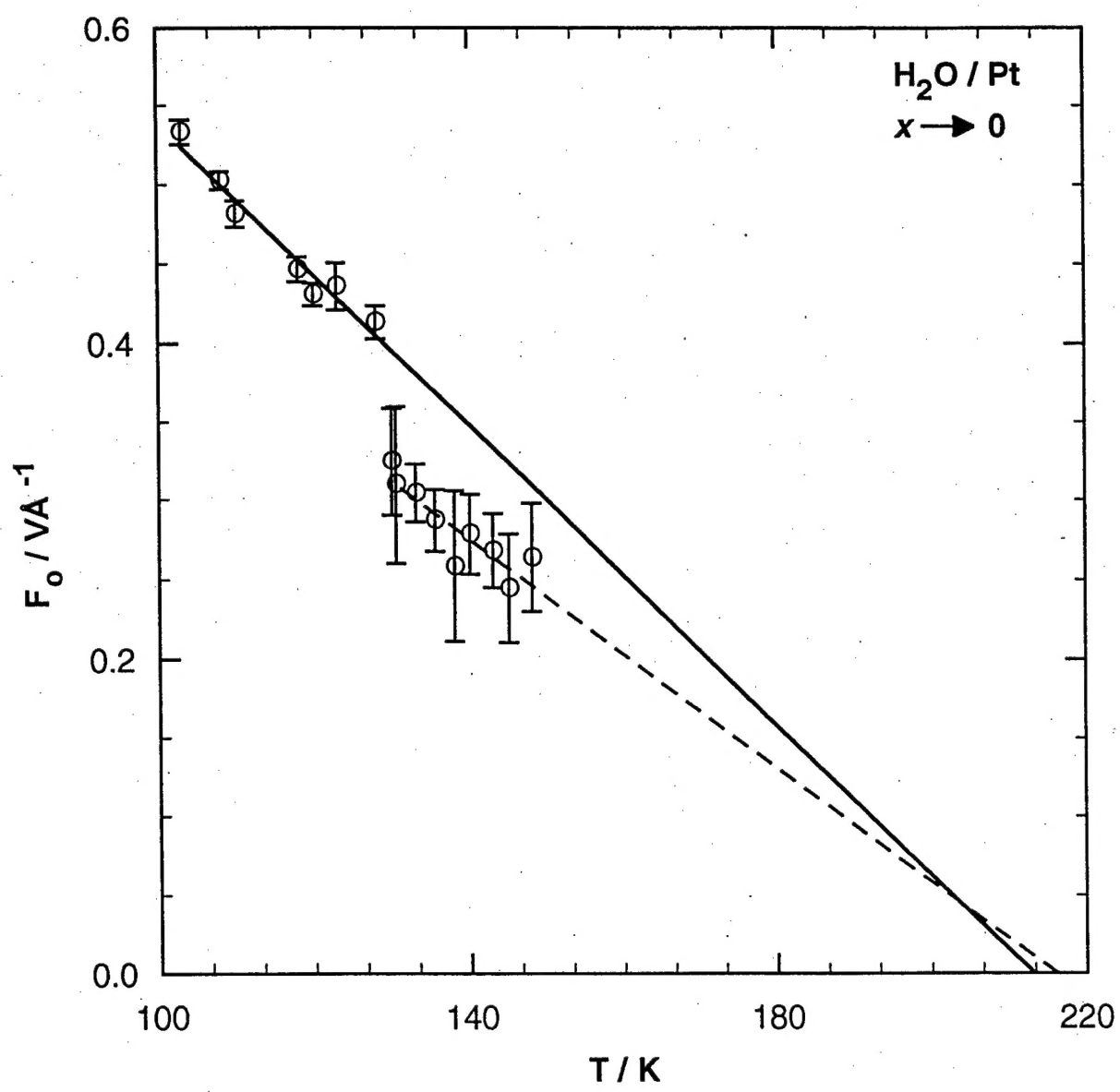


Fig. 11
Scovell et. al.